Zitierweise: *Angew. Chem. Int. Ed.* **2024**, *63*, e202410645
doi.org/10.1002/anie.202410645

Bioimaging

Development of a Dual-Factor Activatable Covalent Targeted Photoacoustic Imaging Probe for Tumor Imaging

Jiho Song[+], Tianqu Zhai[+], Heung Sik Hahm, Yuancheng Li, Hui Mao, Xueding Wang, Janggun Jo, and Jae Won Chang**

Abstract: Photoacoustic imaging (PAI) is an emerging modality in biomedical imaging with superior imaging depth and specificity. However, PAI still has significant limitations, such as the background noise from endogenous chromophores. To overcome these limitations, we developed a covalent activity-based PAI probe, NOx-JS013, targeting NCEH1. NCEH1, a highly expressed and activated serine hydrolase in aggressive cancers, has the potential to be employed for the diagnosis of cancers. We show that NOx-JS013 labels active NCEH1 in live cells with high selectivity relative to other serine hydrolases. NOx-JS013 also presents its efficacy as a hypoxia-responsive imaging probe in live cells. Finally, NOx-JS013 successfully visualizes aggressive prostate cancer tumors in mouse models of PC3, while being negligibly detected in tumors of non-aggressive LNCaP mouse models. These findings show that NOx-JS013 has the potential to be used to develop precision PAI reagents for detecting metastatic progression in various cancers.

[*] Dr. J. Song,[+] Dr. H. S. Hahm, Prof. Dr. J. W. Chang
Department of Pharmacology and Chemical Biology
Emory University
Atlanta, Georgia 30322, United States
E-mail: jae.won.chang@emory.edu

T. Zhai,[+] Prof. Dr. X. Wang, Dr. J. Jo
Department of Biomedical Engineering
University of Michigan
Ann Arbor, MI 48109, USA
E-mail: janggunj@umich.edu

Dr. Y. Li, Prof. Dr. H. Mao
Department of Radiology and Imaging Science
Emory University
Atlanta, Georgia 30322, United States

Prof. Dr. J. W. Chang
Department of Hematology and Medical Oncology
Emory University
Atlanta, Georgia 30322, United States

Prof. Dr. J. W. Chang
Winship Cancer Institute
Emory University
Atlanta, Georgia 30322, United States

[+] These authors contributed equally to this work.

Introduction

The process of diagnosing cancer holds significant importance within the field of oncology. Imaging modalities to detect and quantify cancerous lesions in vivo is a mainstay technology for non-invasive detection, staging, and treatment of human solid tumors.[1–4] Tumor imaging has primarily relied on the use of radiotracers like ^{18}fluorodeoxyglucose (FDG)[5] for positron-emission tomography (PET) imaging. Additional targeting modalities have been explored recently, including glutamine,[6–7] protease substrate mimics,[8–9] and antibodies directed to cancer-associated surface antigens.[10–11] These reagents aim to label cancerous tissue preferentially, providing differential imaging contrast. Two major limitations of most of these agents, including FDG, are poor specificity resulting from background activity in normal tissues and variable residence times bound to the target of interest, which in many cases limits clinical utility. Additionally, metabolic tracers like FDG may show signal loss post-treatment, not consistently reflecting reduced tumor burden but rather transient metabolic suppression, leading to inaccurate treatment assessments. The successes and limitations of these clinical diagnostics validate the need to identify new biological targets associated with cancer as well as molecules capable of targeting them for diagnostic imaging.

Photoacoustic (PA) imaging (PAI) is an emerging modality that has received considerable attention in biomedical imaging,[12–15] specifically cancer imaging.[4,16–19] PAI offers a new clinically translatable imaging modality by combining non-ionizing, deep-penetrating excitation light with acoustic detection.[12,20] By detecting sound rather than emitted light, PAI overcomes the limited imaging resolution of deep tissue associated with fluorescence imaging. Despite these advantages, PAI is adversely affected by ambient noise introduced by endogenous chromophores, such as hemoglobin and melanin. Given cancer's rapid development and increased demand for energy, oxygen, and elevated levels of various metabolic enzymes and metabolites, PAI reagents that take advantage of these characteristics to reduce environmental interference have been reported for tumor imaging.[16] The reagents include mvGlu-AB2, which facilitates GLUT1 for tumor-selective accumulation,[21] AS–Cy-NO_2, which is triggered in hypoxia,[18] BDP-DOH, which ratiometrically detects redox homeostasis,[22] and NRM, a dual-factor activatable PAI probe that is activated by nitric oxide and acidic environments.[23] However, the majority of the activatable PAI reagents rely on single-factor

© 2024 Wiley-VCH GmbH

activation, rendering them susceptible to interference from background noise.[13] Therefore, there is an urgent need for novel approaches to improve the precision specificity of imaging.

To address this need, we hereby describe a covalent targeted PAI reagent with dual-factor activation, specifically engineered to enhance the quality of the images. We show the development of hypoxia activatable PAI reagent that selectively and covalently binds neutral cholesterol ester hydrolase 1 (NCEH1, also known as AADACL1 or KIAA1363), a protein highly expressed and activated in several aggressive cancers.[24–25] The medicinal chemistry effort yielded a highly potent and selective NCEH1 targeting PAI reagent (NOx-JS013) that incorporates the aza-BODIPY chromophore (Figure 1). Subsequently, we comprehensively evaluated the photophysical properties and hypoxic activation of NOx-JS013 as a PAI reagent. Finally, we employed NOx-JS013 to image aggressive tumors in a xenograft mouse model of prostate cancer.

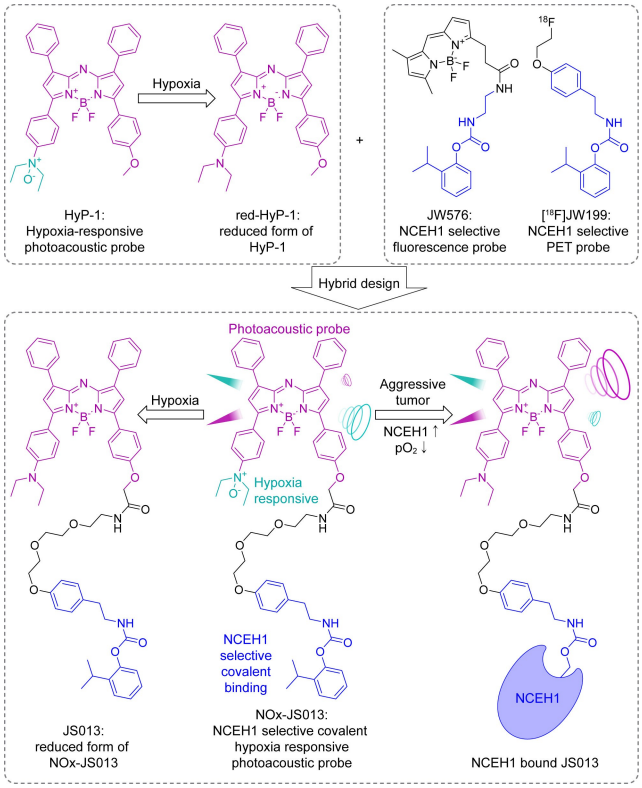


Figure 1. Schematic illustration of hypoxia activatable NCEH1 covalent PAI probe. NOx-JS013 compound was designed based on NCEH1 imaging probes (JW576 and [^{18}F]JW199) and hypoxia-responsive probe HyP-1. In aggressive tumors, NOx-JS013 will label NCEH1 and be reduced to the corresponding amine, becoming a more efficient PA imaging reagent.

Results and Discussion

Design and Synthesis of NOx-JS013 and JS013

Activity-based protein profiling (ABPP) is a chemical proteomic platform that enables the characterization of enzyme activities within their native biological environments.[26–27] The ability to manipulate ABPP in a competitive manner has facilitated the creation of selective inhibitors that can be used to investigate the activity of disease-relevant enzymes in animal and cellular models.[27–32] The specificity of these probes paves the way for the development of new biological applications, one of which is the direct spatial and temporal observation of active enzymes in cells and tissues.[30,33–35] We have recently developed a highly specific fluorescent (JW576)[34] and PET ([^{18}F]JW199)[35] imaging probes targeting a single cancer-associated serine hydrolase, NCEH1 (Figure 1).[24–25,28] This enzyme is present at low levels in most tissues and non-aggressive cancer cells. However, in numerous aggressive and/or metastatic cancers, both the level and the activity of NCEH1 are increased by ~20-fold, thus providing a highly specific marker for metastatic tumor cells.[25,28] Beyond its use as fluorescence and PET imaging probes, JW576 and [^{18}F]JW199 present an exciting opportunity to develop a new class of precision PAI reagents that report on NCEH1(Figure 1). PAI is a powerful imaging modality and an attractive alternative to other common biomedical imaging modalities.[20] Specifically, we are also wondering whether the novel PAI reagents can detect hypoxia at the same time for a synergic effect because rapid and specific hypoxia detection in vivo is of great significance in both preclinical and clinical settings.[36–37]

We are therefore interested in developing novel PAI reagents for NCEH1 activity in tumors, as well as the hypoxia around the tumor microenvironment. For the direct readout of target enzyme activity and hypoxia simultaneously, we sought to design first-generation PAI probes to facilitate several activities, including specific probe labeling of NCEH1 activity in situ (in live cell) and in vivo, non-invasive detection of hypoxia with good resolution and high specificity, and high absorptivity in the near-infrared (NIR) window (650–900 nm) with extensive photostability. Recently, an aza-BODIPY hypoxia PAI probe (HyP-1) was reported[38] (Figure 1). The *N*-oxide trigger on HyP-1 can be reduced in the absence of oxygen by heme proteins such as CYP450 enzymes.[38–40] As highlighted in Figure 1, the core structures of HyP-1 and JW576 are remarkably homologous, which led us to hypothesize that combining these core structures should give selective and irreversible PAI probes against NCEH1 and hypoxia. While NCEH1 levels are significantly elevated in aggressive tumors compared to normal tissues, it is also found in certain normal tissues, particularly the kidney. Hence, the integration of activity-based covalent labeling of NCEH1 with distinct characteristics exclusive to aggressive tumors, such as hypoxia, rather than normal tissues, has the potential to enhance the precision of tumor NCEH1 imaging. To leverage these features, we replaced the BODIPY fluorophore on JW576

© 2024 Wiley-VCH GmbH

with an aza-BODIPY core and also incorporated the aza-BODIPY into [^{18}F]JW199 with diverse linkers for NCEH1 activity and hypoxia detection. (Figure 1, Scheme S1 and S2). We first evaluated the potency and selectivity of the synthesized compounds against the target protein NCEH1 in cell lysates (Figure S1). Among the five compounds, JS013 and JS008 showed selective NCEH1 inhibition, and the labeled JS013 showed a stronger fluorescence signal than JS008. Therefore, JS013 was selected for further studies, and the *N*-oxide analog NOx-JS013 was synthesized.

Photophysical Properties of NOx-JS013 and JS013

Photophysical characterization was sought to ascertain the suitability of NOx-JS013 and JS013 for PAI. The absorbance maximum of NOx-JS013 in chloroform is 668 nm, while the corresponding emission maximum is 693 nm (Figure 2a and Table S1). The extinction coefficient (ε) and quantum yield (Φ) of NOx-JS013 were determined to be $3.15\times10^4\ M^{-1}\cdot cm^{-1}$ and 0.04, respectively (Table S1). The maximum absorption and emission wavelengths of JS013 are 758 nm and 804 nm, respectively (Figure 2a and Table S1). Notably, JS013 exhibits an increase in the extinction coefficient ($\varepsilon = 9.63\times10^4\ M^{-1}\cdot cm^{-1}$) and a decrease in the quantum yield ($\Phi = 0.0015$), both of which suggest an amplified PA signal (Table S1).[38] Since PA signals arise from the non-radiative relaxation of absorbed energy, compounds with lower quantum yields are anticipated to exhibit higher PA signals. Because the aza-BODIPY fluorophore is highly lipophilic and poorly soluble in water, we used Cremophor EL (CrEL), a widely used amphiphilic surfactant, to solubilize in aqueous buffers (e.g. DPBS) for further studies in biological conditions.[41–43] The absorbance and fluorescence spectra were not significantly changed in DPBS (Figure S2). Possible nanoparticle formation in the presence of CrEL was not observed according to the dynamic light scattering (DLS) analysis (Figure S3). NOx-JS013's proposed mechanism of action in aggressive cancer systems involves the covalent labeling of NCEH1 and the reduction of *N*-oxide to the corresponding amine. Thus, the detected PA signal originates from JS013, which is covalently bound to NCEH1. The photophysical characteristics of NOx-JS013 and JS013 are thus highly compatible with our hypothesis and subsequent biological investigations.

NOx-JS013 is stable in EtOH but not in DMSO. While measuring the photophysical properties, we observed the decomposition of NOx-JS013 in DMSO at ambient temperature and reached its complete decomposition after 24 hours (Figure S4a). A significant portion of the decomposed mixture consisted of JS013, while a smaller peak was determined to be BF_2 removed JS013 (Figure S5). We assume that DMSO contributed to the reduction of *N*-oxide as a reducing agent.[44–45] To render the compound stable for

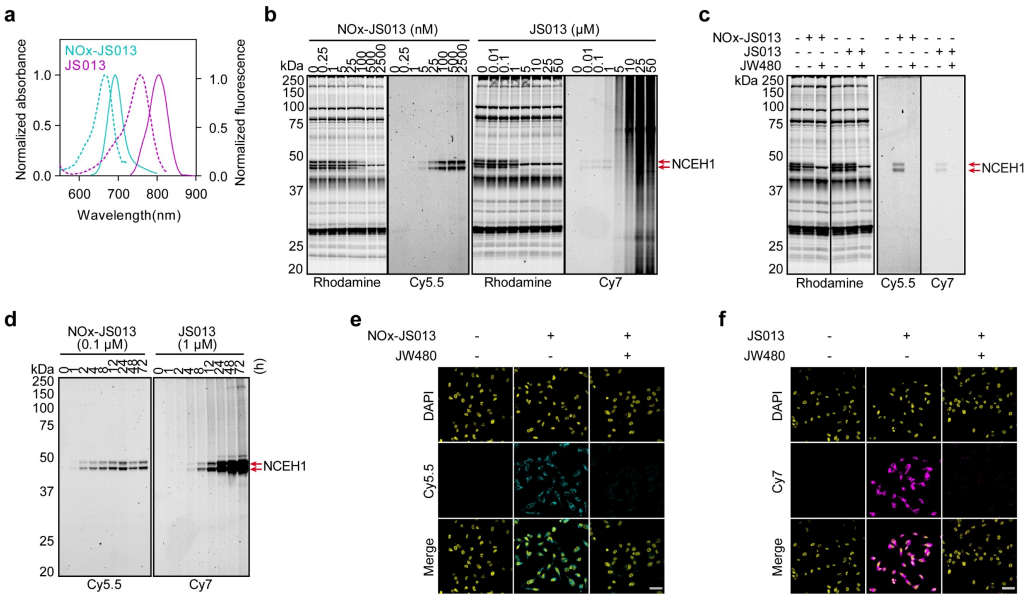


Figure 2. NOx-JS013 and JS013 selectively inhibit NCEH1. **(a)** Absorption (dashed) and emission (solid) spectra of NOx-JS013 (3.75 μM) and JS013 (1.25 μM) in $CHCl_3$. **(b)** Representative competitive ABPP gel image of membrane proteome of in situ dose experiments in PC3 cells. PC3 cells were treated with indicated concentrations of compounds for 4 h. NOx-JS013 signals were imaged at the Cy5.5 channel, and JS013 signals were imaged at Cy7 channel (n = 3). **(c)** Representative competitive ABPP gel image of membrane proteome of in situ competition experiments in PC3 cells. Cells were pretreated with JW480 for 1 h (1 μM) and then treated with JS013 (1 μM) or NOx-JS013 (25 nM) for 4 h. NOx-JS013- and JS013-labeling were blocked by the pretreatment of JW480 (n = 3). **(d)** Representative ABPP gel image of membrane proteome of in situ time-dependent experiments in PC3 cells. For indicated durations, PC3 cells were treated with NOx-JS013 (0.1 μM) or JS013 (1 μM). NOx-JS013 and JS013 time-dependently and selectively labeled NCEH1 (*n* = 3). **(e)** Representative confocal fluorescence image of PC3 cells treated with NOx-JS013 (25 nM) for 4 h with or without pretreatment of JW480 (10 μM) for 4 h. NOx-JS013 selectively labeled NCEH1 in PC3 cells (n = 2, scale bar represents 50 μm). **(f)** Representative confocal fluorescence image of PC3 cells treated with JS013 (1 μM) for 4 h with or without pretreatment of JW480 (10 μM) for 4 h. JS013 selectively labeled NCEH1 in PC3 cells (n = 2, scale bar represents 50 μm).

© 2024 Wiley-VCH GmbH

subsequent characterization, we prepared NOx-JS013 solutions in several polar organic solvents and tested the stability of NOx-JS013 (Figure S4). As a result of these screenings, we determined that NOx-JS013 in EtOH was very stable for up to 48 hours at room temperature (Figure S4d).

Selectivity and Potency of NOx-JS013 and JS013 against NCEH1

We next assessed whether NOx-JS013 and JS013 selectively targeted NCEH1 by using the serine hydrolase-directed probe fluorophosphonate-rhodamine (FP–Rh) in competitive ABPP.[27–30] Prior to conducting in situ experiments, we assessed the cytotoxicity of NOx-JS013 and JS013 in several cancer cells that expressed NCEH1 (Figure S6). Neither NOx-JS013 nor JS013 exhibited noteworthy cytotoxicity at the investigated concentrations. Live cells or cell lysates of PC3, metastatic prostate cancer cells with high endogenous NCEH1 levels, were treated with NOx-JS013 and JS013, then analyzed by gel-based ABPP (Figure 2b and S7).[28,34] NOx-JS013 selectively inhibited NCEH1 with a half maximum inhibitory concentration (IC_{50}) of 53 nM in situ (Figure 2b and S8a). The in vitro (in cell lysate) potency of NOx-JS013 was more than 20-fold lower than its potency in situ (Figure S7a and S8a). The higher potency and selectivity of NOx-JS013 in situ than in vitro highlight the significance of live cell profiling (Figure 2b, S7 and S8). A NOx-JS013-NCEH1 covalent adduct was observed concurrently from the Cy5.5 fluorescence channel, which confirmed that NOx-JS013 inhibited FP–Rh labeling of NCEH1 (Figure 2b). Notably, we detected other NOx-JS013 adducts only at high NOx-JS013 concentrations (Figure 2b). However, JS013 exhibited diminished selectivity and potency in vitro and in situ when compared to NOx-JS013 (Figure 2b, S7b and S8b). We presumed that the low potency and selectivity of JS013 resulted from its low cell permeability. Since the *N*-oxide group is the only distinguishing feature between NOx-JS013 and JS013 (Figure 1 and Scheme S2), we surmised that it only altered cell permeability and not target engagement. We also wanted to confirm that both probes had target-specific labeling via a competition experiment using a highly selective NCEH1 inhibitor, JW480.[28] Pretreatment of PC3 cells with JW480 completely suppressed the NOx-JS013- and JS013-labeled NCEH1 signals (Figure 2c). It was also discovered that NCEH1 inhibition and labeling by NOx-JS013 and JS013 were time-dependent, with target alteration and barely detectable off-target interactions observed after 4 hours in PC3 cells (Figure 2d and S9). Later, NOx-JS013 and JS013 labeled NCEH1 in PC3 cells were visualized by confocal fluorescence microscopy. Confocal fluorescence microscopy images of NOx-JS013- or JS013-treated PC3 cells were acquired using DAPI, Cy5.5, and Cy7 channels to visualize the nucleus, NOx-JS013, and JS013, respectively (Figure 2e and 2f). Strong fluorescence signals were observed in Cy5.5 and Cy7 channels, respectively, in both NOx-JS013 and JS013 treated cells (Figure 2e and 2f). Consistent with the gel-based ABPP experiments (Figure 2c), pretreatment with JW480 blocked these signals (Figure 2e and 2f). These results demonstrated the potency and selectivity of NOx-JS013 and JS013 as imaging probes for NCEH1 in cancer cells.

In vitro and In situ Profiling for Responsiveness to Hypoxia

We first assessed the stability of NOx-JS013 in biological conditions before evaluating the responsiveness to hypoxia in vitro and in situ. Solutions of NOx-JS013 and JS013 in DPBS (pH 7.4) were incubated at ambient light and temperature for 0 to 144 h, and then the fluorescence intensity, absorbance and fluorescence spectra were recorded (Figure S10). Both compounds showed no significant reduction of absorbance or fluorescence intensity even after six days. We also measured absorbance and fluorescence spectra of NOx-JS013 and JS013 in Britton-Robinson buffer with pH ranging from 4 to 12. Even though NOx-JS013 showed slightly decreased absorbance and fluorescence signal intensity at pH 12, both compounds revealed exceptional stability in different pH ranges, especially biological conditions (Figure S11). After confirming the biological stability of both compounds, we measured PA spectra with NOx-JS013 and JS013 throughout the wavelength ranging from 690 nm to 850 nm (Figure 3a). We observed that JS013 showed a robust PA signal at 770 nm wavelength, while a negligible signal was produced by NOx-JS013 at this wavelength. We also imaged the PA signals of NOx-JS013 and JS013 in tubes submerged in water (Figure 3b). Consistent with the PA spectra, JS013 showed a 5.3-fold stronger signal than NOx-JS013 at 770 nm wavelength (Figure 3b and 3c). Notably, NOx-JS013 and JS013 have distinguished absorption/emission spectra (Figure 2a) that can be utilized for ratiometric imaging and spectral unmixing analysis with their PA and fluorescence signals to reduce background signal noise.

We next confirmed that NOx-JS013 effectively responds to hypoxia in vitro and in situ. We performed an in vitro assay by incubating NOx-JS013 with CYP450-rich rat liver microsomes (RLM) under hypoxic conditions given that RLM have been used to study the activation of hypoxia-responsive probes and prodrugs.[38,40,46–48] When NOx-JS013 was incubated with RLM and NADPH under hypoxia, the absorbance spectrum showed a time-dependent decrease of the NOx-JS013 component, while the JS013 component increased (Figure 3d). Consistent with the absorbance spectrum, the fluorescence intensity of the mixture decreased at 640 nm over time and concurrently increased at 760 nm (Figure S12). The PA images from tubes submerged in water also demonstrated that the signal intensity of NOx-JS013 under hypoxia at 770 nm was 7.1-fold stronger than under normoxic conditions (Figure 3e and 3f). These results strongly indicated that NOx-JS013 was converted to JS013 under hypoxia in the presence of CYP enzymes. We examined the Fe^{2+} ion-mediated reduction of NOx-JS013, since a set of dialkyl-arylamine *N*-oxide containing fluorescent probes responsive to Fe^{2+} ions had been previously reported.[49–50] In the presence of Fe^{2+} ions, either with or without the addition of GSH, NOx-JS013 did not show any

© 2024 Wiley-VCH GmbH

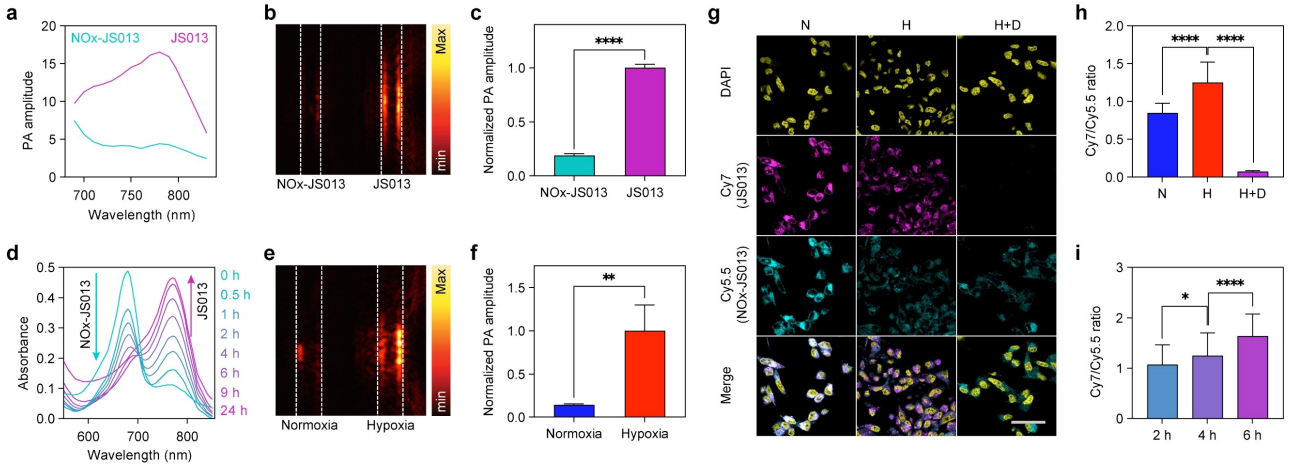


Figure 3. Photoacoustic (PA) signals of JS compounds and reduction of NOx-JS013 in hypoxia. **(a)** PA spectra of NOx-JS013 (50 μM) and JS013 (50 μM) in DPBS. **(b)** Representative PA image of NOx-JS013 (50 μM) and JS013 (50 μM) in tubes submerged in water at 770 nm (n = 3). **(c)** Normalized PA signal intensities of NOx-JS013 (50 μM) and JS013 (50 μM) at 770 nm (n = 3). JS013 showed a 5.3-fold stronger PA signal at 770 nm than NOx-JS013. **(d)** Absorbance spectra of a mixture of NOx-JS013 (5 μM), NADPH (500 μM), and RLM (500 μg/mL) in DPBS. NOx-JS013 was converted to JS013 time-dependently, and near-complete conversion was observed at 24 h. **(e)** Representative PA image of NOx-JS013 (10 μM) after incubation with RLM (1 mg/mL) and NADPH (1 mM) in normoxia or hypoxia for 24 h (n = 3). **(f)** Normalized PA signal intensities of NOx-JS013 (10 μM) at 770 nm after incubation with RLM (1 mg/mL) and NADPH (1 mM) in normoxia or hypoxia for 24 h (n = 3). Hypoxic incubation resulted in a 7.1-fold higher PA signal intensity at 770 nm. **(g)** Representative confocal fluorescence images of PC3 cells treated with NOx-JS013 (25 nM) for 4 h in normoxia and hypoxia and PC3 cells treated with both NOx-JS013 (25 nM) and DPI (500 μM) incubated in hypoxia for 4 h. In-cell conversion of NOx-JS013 to JS013 was inhibited by pan CYP inhibitor DPI (n = 3, scale bar represents 50 μm). **(h)** The ratio of signal intensities at Cy7 channel (JS013) to Cy5.5 channel (NOx-JS013) in cells. **(i)** The ratio of signal intensities at Cy7 channel (JS013) to Cy5.5 channel (NOx-JS013) in cells. N: Normoxia, H: Hypoxia, H + D: Hypoxia + DPI, Data were presented as means with SD. Statistical analyses were performed via Student's *t*-test. $*p < 0.05$, $**p < 0.01$, $****p < 0.0001$.

ratiometric turn-on response (Figure S13). Additionally, we assessed whether the NOx-JS013 could be turned on by reactive oxygen, nitrogen, sulfur, or metal species that are frequently encountered in the cellular environment. We confirmed that NOx-JS013 had no ratiometric turn-on response, indicating that it was not converted to JS013 under these conditions (Figure S14).

In order to determine whether heme-based redox proteins, such as CYP450 reductases, are specifically responsible for the hypoxic response of NOx-JS013 in live cells, we sought to inhibit CYP450 enzyme activity by adding diphenyliodonium chloride (DPI).[51] Therefore, ratiometric fluorescence imaging experiments were conducted by subjecting PC3 cells to treatment with NOx-JS013 (25 nM) in the presence or absence of DPI (500 μM) and incubating them at 37 °C for 4 hours under normoxic or hypoxic conditions. At the same time, we further validated the system using HyP-1 and a commercial hypoxia probe,[52] beyond the Anaero-Indicator, since the hypoxia cell culture system was crucial for the experiment (Figure S15). We observed NOx-JS013 and JS013 fluorescence signals with Cy7 and Cy5.5 channels, respectively, and subsequently quantified each fluorescence signal. The ratiometric fluorescence signal in cells cultured under hypoxic conditions was approximately 1.5-fold higher than in normoxic conditions (Figure 3g and 3h). Notably, we observed that the reduction of NOx-JS013 to JS013 did not occur under hypoxic conditions when CYP450 activity was inhibited by DPI (Figure 3g and 3h). We were able to confirm that the CYP450 enzymes are the primary reducing factor for NOx-JS013 in vitro as well as in situ. In addition, we found that the ratiometric fluorescence response to hypoxia demonstrated a time-dependent increase (Figure 3i and S16). These results, combined with the lower potency and slower inhibition rate of JS013 in situ compared to NOx-JS013, indicate that the majority of NOx-JS013 compounds bind to NCEH1 first and then the *N*-oxide is reduced to the corresponding amine, rather than being reduced first, and then binding to NCEH1. We also observed a decrease of signal intensity of NOx-JS013 in Cy7 channel under hypoxic conditions (Figure 3g). In the control experiment using HyP-1, we also observed lower signal intensity in Cy7 channel under hypoxic conditions compared to normoxic conditions (Figure S15b and S15c). We assume that interaction of probes with unknown proteins under hypoxia affected the fluorescence intensity.

In vivo Tumor Imaging with NOx-JS013

Next, we aimed to evaluate our compound as a PAI reagent for in vivo tumor imaging. Before proceeding with in vivo experiments, we assessed potential hemolytic toxicity of NOx-JS013 and JS013. Both compounds did not induce significant hemolysis in mouse red blood cells (Figure S17). Although our probe possesses a dual-wavelength ratiometric feature for PA imaging, ratiometric imaging can be interfered with by substantial signals from background tissues. In

© 2024 Wiley-VCH GmbH

the NIR wavelength region, the optical absorption of hemoglobin is sufficient to affect ratiometric PAI.[53] To reduce the background signals interference, we used the PA spectral unmixing method that enables precise calculation of relative concentrations of NOx-JS013, JS013, oxyhemoglobin, and deoxyhemoglobin. When most PA signals are generated by these four chromophores, spectral unmixing techniques can decompose the mixed PA signals into the four constituents in each pixel with multiple PA images obtained from different wavelengths (Supporting Information).[54] In addition to 690 nm and 770 nm which can be used for ratiometric processing, four more wavelengths (736, 756, 797, and 830 nm) were selected based on the absorption spectra of NOx-JS013, JS013, oxyhemoglobin, and deoxyhemoglobin. The phantom study showed that the PA signal of each of these four molecules could be successfully extracted from the mixtures of these molecules (Figure S18).

PC3 xenograft mouse models were employed for the tumor imaging to compare the amounts of NOx-JS013 and JS013, using the image processing method. NOx-JS013 was administered to mice with PC3 tumors reaching around 1 cm^3 through IV injection. Then, the tumors were imaged just before the injection and at 1 and 6 hours after administration. The mice's thigh muscles were also imaged as a control group. After PA spectral unmixing, we obtained the representative PA images showing relative concentrations of NOx-JS013 and JS013 in the tumor and thigh regions (Figure 4a and 4c). The PA images displaying the concentrations of NOx-JS013 and JS013 with the color scale were overlapped on the gray-scaled ultrasound (US) images. At 1 h after administration of NOx-JS013, the PA image intensities of NOx-JS013 and JS013 in tumor regions were not significantly different. However, at 6 h, a significantly higher concentration of JS013 than NOx-JS013 was observed in the tumors ($p = 0.0018$ from a paired t-test), while the average concentrations of NOx-JS013 and JS013 were similar in the thigh muscles ($p = 0.85$ from a paired t-test, Figure 4b and 4d). Unlike the tumor region, the signals of both compounds in the thigh region fluctuated and showed no clear tendency (Figure 4d). Spectral unmixing of PA signals from six wavelengths gave better images than ratiometric processing of PA signals from dual-wavelength, 770 nm and 690 nm (Figure S19). Spectral unmixing (ratio of unmixed signal intensities of JS013 to NOx-JS013) showed 14.1-fold increase at 6 h from 0 h in the tumor region, while ratiometric processing showed only 1.6-fold increase (ratio of signal intensities at 770 nm to 690 nm). These results indicate that our spectral unmixing method is better suited for the current study (Figure 4a, 4b, S19a, and S19b).

To verify the tumor selectivity of NOx-JS013, we collected several organs and assessed the fluorescence of each organ ex vivo (Figure S20). The average signal intensity of JS013 was greater in the tumor compared to the brain, heart, and spleen. Furthermore, the JS013/NOx-JS013 ratio was much higher in the tumor (8.2-fold) than in the lung (5.0-fold), while both NOx-JS013 and JS013 had strong signal intensities in the lung (Figure S20a and S20b). Since the high levels of NCEH1 expression in the kidney are well known,[35] the strong signal intensity of NOx-JS013 was expected. However, it is noteworthy that the kidney showed a strong signal of JS013 and, the JS013/NOx-JS013 ratio was somewhat higher than the tumor (Figure S20a and S20b). We assumed that high expression levels of CYP enzymes in the kidney caused a substantial reduction of NOx-JS013 into JS013.[55] These data indicate that the biodistribution profile is strongly linked with the in vivo fluorescence signal and relative NCEH1 or CYP450 mRNA abundance in each

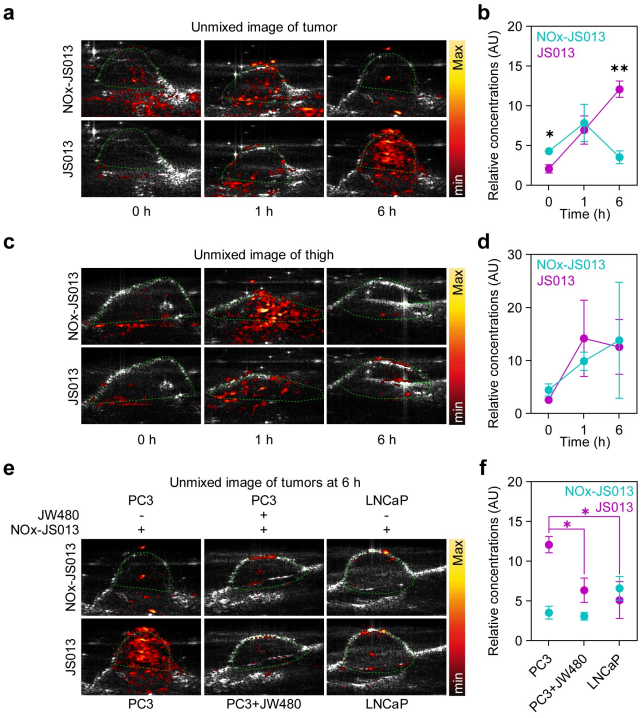


Figure 4. In vivo tumor imaging using NOx-JS013. After NOx-JS013 (20 mg/kg, IV injection) was administered, ultrasound (US) and PA signals were recorded from PC3 or LNCaP xenograft model mice. With the developed PA unmixing method, relative concentrations of NOx-JS013 and JS013 were obtained and visualized as images and quantification graphs. **(a)** Representative US images (gray-scaled) of tumors and unmixed PA images (color scaled) of NOx-JS013 and JS013 in the tumors of PC3 mouse models (n = 6). **(b)** The unmixed signal intensities of NOx-JS013 and JS013 from PC3 tumors ($n = 6$). The signal intensity of JS013 gradually increased in tumors, while that of NOx-JS013 showed a peak at 1 h and decreased. **(c)** Representative US images of thighs and unmixed PA images of NOx-JS013 and JS013 in the thighs of PC3 mouse models (n = 6). **(d)** The unmixed signal intensities of NOx-JS013 and JS013 from mouse thighs ($n = 6$). The signal intensity of NOx-JS013 gradually increased in thighs, while that of JS013 showed a peak at 1 h and slightly decreased. **(e)** Representative unmixed PA images of NOx-JS013 and JS013 from tumors of different mouse models at 6 h after injection of NOx-JS013 (20 mg/kg, IV injection). PC3 mouse models were pretreated with JW480 (80 mg/kg, oral administration) for 4 h before the injection of NOx-JS013 (PC3: n = 6, PC3 + JW480: n = 5, LNCaP: n = 4). Pretreatment of JW480 significantly reduced the JS013 signal intensity. JS013 signal was hardly detected in non-aggressive prostate cancer models, LNCaP. **(f)** The unmixed signal intensities of NOx-JS013 and JS013 from the three groups of mouse tumors (PC3: $n = 6$, PC3 + JW480: $n = 5$, LNCaP: $n = 4$). Data were presented as means with SEM. Statistical analyses were performed via Student's t-test. $^*p < 0.05$, $^{**}p < 0.01$.

© 2024 Wiley-VCH GmbH

tissue. Overall, NOx-JS013 showed high selectivity against tumor compared to normal tissues, except kidney.

To further validate NCEH1 selective labeling with the biotransformation of NOx-JS013 to JS013 in live animals, we performed the in vivo tumor imaging using non-aggressive LNCaP mouse models and PC3 mouse models pretreated with JW480.[56] For competition experiments, JW480 (80 mg/kg, 4 h) was pre-administrated to PC3 mouse models, and then NOx-JS013 was injected through the tail vein. After the same imaging process, we compared the PA images obtained from PC3 tumors, JW480 pretreated PC3 tumors, and LNCaP tumors at 6 h after NOx-JS013 administration. JS013 PA signal intensities from tumor regions of both JW480 pretreated PC3 tumors and LNCaP tumors were significantly lower than the PA signal of JS013 in PC3 tumors ($p = 0.011$ and 0.014, respectively, from unpaired t-test, Figure 4e and 4f). The results of the competition experiments demonstrate the signal enhancement by the covalent NCEH1 labeling function.

Conclusion

We have developed a covalent targeted PAI reagent, NOx-JS013, with dual-factor activation designed to enhance imaging capability. This innovative reagent combines the activity-based covalent targeting of NCEH1, a protein highly expressed in aggressive cancers, with responsiveness to hypoxia. The probes NOx-JS013 and its hypoxia-activated form JS013 were thoroughly evaluated for potency and specificity against NCEH1 using ABPP. NOx-JS013 demonstrated outstanding selectivity and potency in live cell systems rather than in cell lysate, emphasizing the importance of live cell profiling for precise imaging reagent evaluation. Photophysical characterization of NOx-JS013 and JS013 revealed their suitability for PAI, with absorbance and emission wavelengths falling within the desired range for practical imaging. Specifically, the enhanced PA signal of JS013 indicated its potential for generating high-quality images. The hypoxia responsiveness of NOx-JS013 was confirmed through in vitro experiments.

The conversion of NOx-JS013 into JS013 under hypoxia was further validated in situ, thereby establishing its efficacy as a hypoxia-responsive imaging probe. The probes demonstrated exceptional stability in biological buffers, making them reliable tool compounds for hypoxia detection. In vivo tumor imaging using NOx-JS013 showed promising results with strong signals observed in the tumor region. The gradual increase in JS013 signal over time indicated successful biotransformation of NOx-JS013 in response to hypoxia. The in vivo experiments in non-aggressive LNCaP mouse models and the competition experiments using JW480, an inhibitor of NCEH1, in PC3 mouse models further supported the specificity of the imaging signals to NCEH1.

Although further studies will be essential to validate the effectiveness of NOx-JS013 in clinical applications, the basic concept we present here might also be extended to other target proteins highly expressed or activated in aggressive cancers. Furthermore, a significant obstacle in detecting metastasis with other imaging reagents is the presence of elevated background signals in the target organs. This is a significant challenge in malignancies that frequently exhibit metastasis to other organs. Our approach can also be utilized to develop innovative PAI probes that provide information on a newly discovered biomarker associated with metastasis.

Overall, this study introduces NOx-JS013 as a novel PAI reagent. This reagent utilizes both activity-based covalent targeting of NCEH1 and ratiometric hypoxia responsiveness simultaneously. This novel approach demonstrated enhanced sensitivity and specificity in aggressive tumor imaging by effectively reducing background noise signals from endogenous chromophores. Thus, NOx-JS013 highlights our innovative approach of employing covalent targeting along with dual-factor activation to improve the imaging of aggressive tumors. Furthermore, this strategy addresses the limitations of current imaging techniques and provides a valuable tool for accurate cancer diagnosis and treatment monitoring.

Supporting Information

The authors have cited additional references within the Supporting Information.

Acknowledgements

This work was supported by the National Cancer Institute (R01CA250499), Prostate Cancer Foundation (19YOUN12), and the Winship Cancer Institute (NIH 5P30CA138292). The research reported in this publication was supported in part by the Emory University Integrated Cellular Imaging Core of the Winship Cancer Institute of Emory University and NIH/NCI under award number, 2P30CA138292-04, (RRID:SCR_023534). The content is solely the responsibility of the authors and does not necessarily reflect the official views of the National Institute of Health. We thank the Read Lab at Emory University, especially Dr. Gee Young Lee, for providing mouse blood for hemolytic toxicity experiments. We thank the Chang lab and the Wang lab for helpful discussions. The Table of Contents graphical abstract was partially created with BioRender.com.

Conflict of Interest

The authors declare no conflict of interest.

Data Availability Statement

The data that support the findings of this study are available from the corresponding author upon reasonable request.

© 2024 Wiley-VCH GmbH

Keywords: Photoacoustic imaging · Tumor imaging · Covalent probe · NCEH1 · Hypoxia

[1] S. Hernot, L. van Manen, P. Debie, J. S. D. Mieog, A. L. Vahrmeijer, *Lancet Oncol.* **2019**, *20*, e354–e367.
[2] J. V. Frangioni, *J. Clin. Oncol.* **2008**, *26*, 4012–4021.
[3] A. S. Thakor, S. S. Gambhir, *Ca-Cancer J. Clin.* **2013**, *63*, 395–418.
[4] S. Mallidi, G. P. Luke, S. Emelianov, *Trends Biotechnol.* **2011**, *29*, 213–221.
[5] K. Paydary, S. M. Seraj, M. Z. Zadeh, S. Emamzadehfard, S. P. Shamchi, S. Gholami, T. J. Werner, A. Alavi, *Mol. Imaging Biol.* **2019**, *21*, 1–10.
[6] S. Venneti, M. P. Dunphy, H. W. Zhang, K. L. Pitter, P. Zanzonico, C. Campos, S. D. Carlin, G. La Rocca, S. Lyashchenko, K. Ploessl, D. Rohle, A. M. Omuro, J. R. Cross, C. W. Brennan, W. A. Weber, E. C. Holland, I. K. Mellinghoff, H. F. Kung, J. S. Lewis, C. B. Thompson, *Sci. Transl. Med.* **2015**, *7*, 274ra17.
[7] L. Zhu, K. Ploessl, R. Zhou, D. Mankoff, H. F. Kung, *J. Nucl. Med.* **2017**, *58*, 533–537.
[8] Y. Yang, H. Hong, Y. Zhang, W. Cai, *Cancer Growth Metastasis* **2009**, *2*, 13–27.
[9] M. Vizovisek, R. Vidmar, M. Drag, M. Fonovic, G. S. Salvesen, B. Turk, *Trends Biochem. Sci.* **2018**, *43*, 829–844.
[10] G. A. M. S. van Dongen, A. J. Poot, D. J. Vugts, *Tumor Biol.* **2012**, *33*, 607–615.
[11] Z. Szabo, E. Mena, S. P. Rowe, D. Plyku, R. Nidal, M. A. Eisenberger, E. S. Antonarakis, H. Fan, R. F. Dannals, Y. Chen, R. C. Mease, M. Vranesic, A. Bhatnagar, G. Sgouros, S. Y. Cho, M. G. Pomper, *Mol. Imaging Biol.* **2015**, *17*, 565–574.
[12] S. Manohar, S. S. Gambhir, *Photoacoustics* **2020**, *19*, 100196.
[13] Y. Liu, L. Teng, B. Yin, H. Meng, X. Yin, S. Huan, G. Song, X. B. Zhang, *Chem. Rev.* **2022**, *122*, 6850–6918.
[14] S. Wang, Z. Sheng, Z. Yang, D. Hu, X. Long, G. Feng, Y. Liu, Z. Yuan, J. Zhang, H. Zheng, X. Zhang, *Angew. Chem. Int. Ed.* **2019**, *58*, 12415–12419.
[15] P. Cheng, W. Chen, S. Li, S. He, Q. Miao, K. Pu, *Adv. Mater.* **2020**, *32*, 1908530.
[16] Z. X. Zhao, C. B. Swartchick, J. Chan, *Chem. Soc. Rev.* **2022**, *51*, 829–868.
[17] C. Qiu, Y. Bai, T. Yin, X. Miao, R. Gao, H. Zhou, J. Ren, L. Song, C. Liu, H. Zheng, R. Zheng, *BMC Cancer* **2020**, *20*, 419.
[18] S. Zhang, H. Chen, L. Wang, X. Qin, B. P. Jiang, S. C. Ji, X. C. Shen, H. Liang, *Angew. Chem. Int. Ed.* **2022**, *61*, e202107076.
[19] S. H. Gardner, C. J. Brady, C. Keeton, A. K. Yadav, S. C. Mallojjala, M. Y. Lucero, S. Su, Z. Yu, J. S. Hirschi, L. M. Mirica, J. Chan, *Angew. Chem. Int. Ed.* **2021**, *60*, 18860–18866.
[20] L. V. Wang, S. Hu, *Science* **2012**, *335*, 1458–1462.
[21] A. K. East, M. C. Lee, C. Jiang, Q. Sikander, J. F. R. Chan, *J. Am. Chem. Soc.* **2023**, *145*, 7313–7322.
[22] J. D. Zheng, Q. Zeng, R. J. Zhang, D. Xing, T. Zhang, *J. Am. Chem. Soc.* **2019**, *141*, 19226–19230.
[23] L. L. Teng, G. S. Song, Y. C. Liu, X. Y. Han, Z. Li, Y. J. Wang, S. Huan, X. B. Zhang, W. H. Tan, *J. Am. Chem. Soc.* **2019**, *141*, 13572–13581.
[24] K. P. Chiang, S. Niessen, A. Saghatelian, B. F. Cravatt, *Chem. Biol.* **2006**, *13*, 1041–1050.
[25] D. K. Nomura, J. Z. Long, S. Niessen, H. S. Hoover, S. W. Ng, B. F. Cravatt, *Cell* **2010**, *140*, 49–61.
[26] N. Jessani, Y. S. Liu, M. Humphrey, B. F. Cravatt, *Proc. Natl. Acad. Sci. USA* **2002**, *99*, 10335–10340.
[27] B. F. Cravatt, A. T. Wright, J. W. Kozarich, *Annu. Rev. Biochem.* **2008**, *77*, 383–414.
[28] J. W. Chang, D. K. Nomura, B. F. Cravatt, *Chem. Biol.* **2011**, *18*, 476–484.
[29] J. W. Chang, M. J. Niphakis, K. M. Lum, A. B. Cognetta 3rd, C. Wang, M. L. Matthews, S. Niessen, M. W. Buczynski, L. H. Parsons, B. F. Cravatt, *Chem. Biol.* **2012**, *19*, 579–588.
[30] J. W. Chang, A. B. Cognetta 3rd, M. J. Niphakis, B. F. Cravatt, *ACS Chem. Biol.* **2013**, *8*, 1590–1599.
[31] A. B. Cognetta 3rd, M. J. Niphakis, H. C. Lee, M. L. Martini, J. J. Hulce, B. F. Cravatt, *Chem. Biol.* **2015**, *22*, 928–937.
[32] A. F. Kornahrens, A. B. Cognetta 3rd, D. M. Brody, M. L. Matthews, B. F. Cravatt, D. L. Boger, *J. Am. Chem. Soc.* **2017**, *139*, 7052–7061.
[33] J. Fan, S. Guo, S. Wang, Y. Kang, Q. Yao, J. Wang, X. Gao, H. Wang, J. Du, X. Peng, *Chem. Commun.* **2017**, *53*, 4857–4860.
[34] J. W. Chang, R. E. Moellering, B. F. Cravatt, *Angew. Chem. Int. Ed.* **2012**, *51*, 966–970.
[35] J. W. Chang, M. Bhuiyan, H. M. Tsai, H. J. Zhang, G. Li, S. Fathi, D. C. McCutcheon, L. Leoni, R. Freifelder, C. T. Chen, R. E. Moellering, *Angew. Chem. Int. Ed.* **2020**, *59*, 15161–15165.
[36] K. Ruan, G. Song, G. Ouyang, *J. Cell. Biochem.* **2009**, *107*, 1053–1062.
[37] C. Wigerup, S. Påhlman, D. Bexell, *Pharmacol. Ther.* **2016**, *164*, 152–169.
[38] H. J. Knox, J. Hedhli, T. W. Kim, K. Khalili, L. W. Dobrucki, J. Chan, *Nat. Commun.* **2017**, *8*, 1794.
[39] C. R. Nishida, P. R. O. de Montellano, *J. Med. Chem.* **2008**, *51*, 5118–5120.
[40] D. Kang, S. T. Cheung, A. Wong-Rolle, J. Kim, *ACS Cent. Sci.* **2021**, *7*, 631–640.
[41] A. Kamkaew, K. Burgess, *Chem. Commun.* **2015**, *51*, 10664–10667.
[42] D. Frath, P. Didier, Y. Mély, J. Massue, G. Ulrich, *ChemPhotoChem* **2017**, *1*, 109–112.
[43] J. Murtagh, D. O. Frimannsson, D. F. O'Shea, *Org. Lett.* **2009**, *11*, 5386–5389.
[44] M. E. C. Biffin, J. Miller, D. B. Paul, *Tetrahedron Lett.* **1969**, 1015–1018.
[45] M. E. C. Biffin, G. Bockstei, J. Miller, D. B. Paul, *Aust. J. Chem.* **1974**, *27*, 789–799.
[46] R. B. P. Elmes, *Chem. Commun.* **2016**, *52*, 8935–8956.
[47] L. H. Patterson, *Cancer Metastasis Rev.* **1993**, *12*, 119–134.
[48] D. L. Kirkpatrick, H. L. Schroeder, K. J. Chandler, *Anti-Cancer Drugs* **1994**, *5*, 467–472.
[49] T. Hirayama, H. Tsuboi, M. Niwa, A. Miki, S. Kadota, Y. Ikeshita, K. Okuda, H. Nagasawa, *Chem. Sci.* **2017**, *8*, 4858–4866.
[50] M. Niwa, T. Hirayama, K. Okuda, H. Nagasawa, *Org. Biomol. Chem.* **2014**, *12*, 6590–6597.
[51] D. G. Tew, *Biochemistry* **1993**, *32*, 10209–10215.
[52] P. Phukhum, J. Phetcharaburanin, K. Chaleekarn, Y. Kittirat, T. Kulthawatsiri, N. Namwat, W. Loilome, N. Khuntikeo, A. Titapun, A. Wangwiwatsin, T. Khampitak, M. Suksawat, P. Klanrit, *Sci. Rep.* **2023**, *13*, 3072.
[53] J. Jo, C. H. Lee, R. Kopelman, X. D. Wang, *Nat. Commun.* **2017**, *8*, 471.
[54] L. F. Portugal, J. J. Judice, L. N. Vicente, *Math. Comput.* **1994**, *63*, 625–643.
[55] I. Elfaki, R. Mir, F. M. Almutairi, F. M. A. Duhier, *Asian Pacific J. Cancer Prev.* **2018**, *19*, 2057–2070.
[56] D. J. Lim, X. L. Liu, D. M. Sutkowski, E. J. Braun, C. Lee, J. M. Kozlowski, *Prostate* **1993**, *22*, 109–118.

Manuscript received: June 5, 2024
Accepted manuscript online: June 27, 2024
Version of record online: August 14, 2024

© 2024 Wiley-VCH GmbH